ARTICLE

Implanting H_xYO_{2-x} sites into Ru-doped graphene and oxygen vacancies for low-overpotential alkaline hydrogen evolution

Xiang Li[1], Wei Deng[1], Yun Weng[2], Jingjing Zhang[1], Haifang Mao[1], Tiandong Lu[1], Wenqian Zhang[1],
Renqiang Yang[3] and Fei Jiang [1]

Abstract

Highly efficient electrocatalysts for the hydrogen evolution reaction (HER) are essential for sustainable hydrogen energy. The controllable production of hydrogen energy by water decomposition depends heavily on the catalyst, and it is extremely important to seek sustainable and highly efficient water-splitting electrocatalysts for energy applications. Herein, bimetallic $RuYO_{2-x}$ nanoparticles (Ru: 8.84 at.% and Y: 13 at.%) with high densities and low loadings were synthesized and anchored on graphene through a simple solvothermal strategy by synthesizing hydrogen yttrium ketone (H_xYO_{2-x}) serving as an inserted medium. Electron microscopy demonstrated that the $RuYO_{2-x}$/C was composed of densely arranged particles and graphene flakes. Electrochemical results showed that the $RuYO_{2-x}$/C had a remarkably low overpotential of $\eta_{10} = 56$ mV at a current density of 10 mA cm^{-2} in alkaline media, a Tafel slope of 63.18 mV dec^{-1}, and 24 h of stability. The oxygen vacancies of $RuYO_{2-x}$/C provided a large proton storage capacity and a strong tendency to bind hydrogen atoms. DFT calculations showed that $RuYO_{2-x}$/C catalysts with more Ru-O-Y bonds and V_O dramatically decreased the energy barrier for breaking H-OH bonds. Moreover, the robust metal-support interactions provided optimized energies for hydrogen adsorption and desorption, which explained the high activity and favorable kinetics for $RuYO_{2-x}$/C catalytic hydrogen precipitation in alkaline electrolyte reactions. This work presents a hydrogen insertion method for the preparation of low-loading, high-density, high-performance and stable water decomposition catalysts for hydrogen production.

Introduction

The renewable and nonpolluting nature of hydrogen energy has aroused the enthusiasm of researchers owing to the limited fossil energy available on earth and the increasing demand for renewable energy sources[1–3]. Electrochemical water decomposition is regarded as an ideal approach that is essential for future carbon-neutral processes and sustainable energy systems[4,5]. A typical water spitting system has an anodic oxygen evolution

reaction (OER: $4OH^- \rightarrow O_2 + 2H_2O + 4e^-$) and a cathodic hydrogen evolution reaction (HER: $2H_2O + 2e^- \rightarrow H_2 + 2OH^-$) in an alkaline medium with a dynamic potential of 1.23 V[6]. However, the sluggish reaction kinetics often result in a high overpotential and a highly efficient and durable electrocatalyst is especially needed to improve the energy conversion efficiencies[7–12].

Until now, the most effective electrocatalysts are still noble metal-based RuO_2, IrO_2 and Pt/C[13], but their high costs, scarcities and instabilities have greatly hindered their use in a wide range of applications[14–19]. Considering these challenges, the use of nonnoble metals would reduce the dosages of the noble metals and enhance the catalytic activity owing to a synergistic electronic effect or generate defect effects. Surprisingly, these defects could

Correspondence: Wei Deng (wdeng@sit.edu.cn) or
Haifang Mao (maohaifang2000@126.com) or Fei Jiang (jiangfei@sit.edu.cn)
[1]School of Chemical and Environmental Engineering, Shanghai Institute of Technology, 201418 Shanghai, China
[2]State Key Laboratory for Modification of Chemical Fibers and Polymer Materials, College of Textile, Donghua University, 201620 Shanghai, China
Full list of author information is available at the end of the article

alter the local electronic structure and serve as "docking" sites to trap atomic metal species and form new coordination structures for the active sites[20]. Consequently, it is essential to obtain in-depth insight into the roles of defective sites in engineering the electrocatalytic energy conversion process, which would be particularly important in guiding the designs of ideal catalysts[21]. Among the three noble metals used, Ru-based materials are especially promising catalysts for hydrogen production from water splitting because their binding strengths with hydrogen are similar to those of Pt, and they exhibit high HER activity[22]. Previous strategies for enhancing the HER in alkaline media were focused on facilitating the sluggish water dissociation reactions by incorporating a specific component (e.g., a transition metal hydroxide) onto the catalytically active species (e.g., Ru) or inducing surface reconstruction to generate more activity[23]. Yttrium (Y) is a rare earth element, and it exhibits appreciable electrical conductivity and a unique 4 f electron layer, which improves the performance in hydrogen production from electrolytic water splitting when combined with Ru active sites[24,25]. Furthermore, the ionic radius of Y is smaller than that of Ru, which can promote oxygen vacancies as well as structural changes[26].

Although noble metal-based electrocatalysts such as Pt are ideal materials for the HER, alloyed materials[27-29] have been used to provide improved activity[30]. Among the metal-based catalysts used as HER catalysts, carbon is utilized as the catalyst support[31,32] owing to its good conductivity and to avoid agglomeration of the active catalysts for long-term use[33]. Great effort has been expended to utilize nonmetal catalysts, including carbon-related materials such as graphene-doped graphenes[34-36] and graphitic carbon nitride (g-C_3N_4)[37-39]. Alloying is an important way to improve the performance of a catalyst and is commonly used to prepare precious metal-based catalysts[40]. In this study, we present an effective strategy for remarkably enhancing the H coverage on a catalyst for the HER in alkaline media. Specifically, ruthenium-yttrium nanocomposites ($RuYO_{2-x}$) were loaded onto a graphene system rich in oxygen vacancies, and the protons inserted into H_xYO_{2-x} were transferred to $RuYO_{2-x}$/C during the HER and greatly increased the hydrogen coverage on $RuYO_{2-x}$/C and improved the HER performance. Meticulous characterization, including electron paramagnetic resonance (EPR) studies, confirmed robust coupling of the Ru sites with oxygens near the yttrium vacancies. The Ru atomic content was 8.84 at%, which greatly decreased the cost of the noble-metal content compared with those of commercial Ru/C and Pt/C. DFT calculations revealed that the d-band center of Ru might be adjusted closer to the Fermi level due to the synergistic effects of the Y-O-Ru bonds and V_o, which lowered the energy barrier for water dissociation and facilitated the adsorption of water.

Results and discussion
Morphologies and structures

Tunable bimetallic nanocomposites $RuYO_{2-x}$ were loaded on graphene ($RuYO_{2-x}$/C) via a solvothermal method, as shown in Fig. 1, which utilized two metal precursors: a ruthenium salt ($RuCl_3$) and a yttrium precursor (H_xYO_{2-x}) grown on the two-dimensional graphene nanosheets. In particular, the unique low-temperature solution-processed hydrogen yttrium bronze (HMOs) H_xYO_{2-x} was synthesized through a controllable hydrogen insertion method. The yttrium powder was oxidized by hydrogen peroxide in the presence of ethanol. With the reaction rate controlled by ethanol, H_xYO_{2-x} was readily obtained (Supplementary
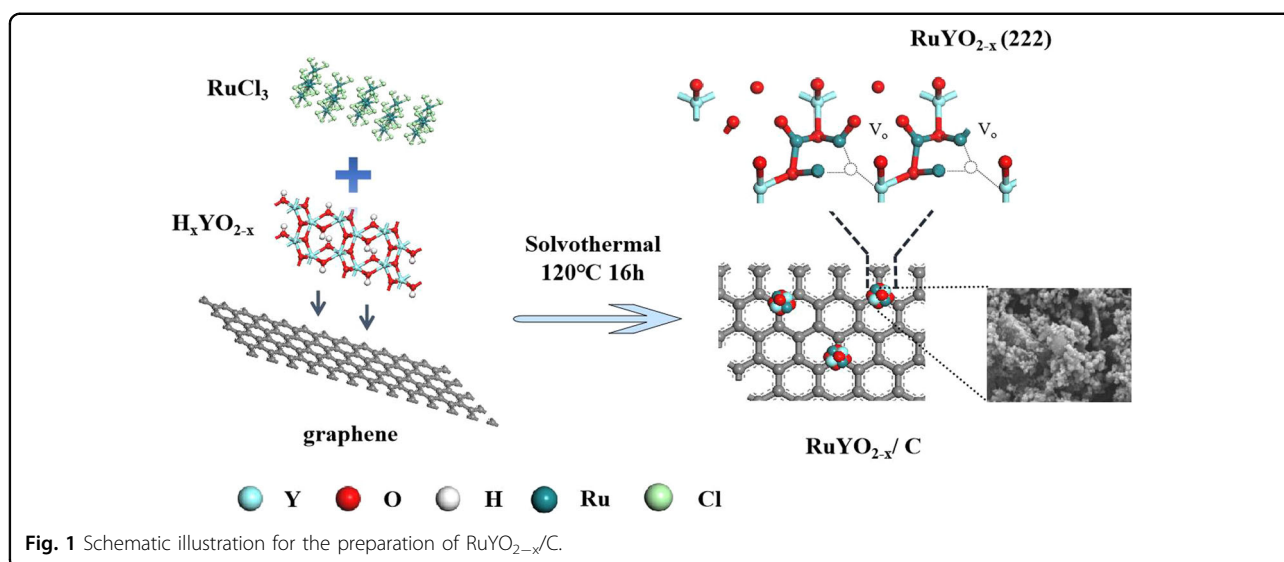
Fig. 1 Schematic illustration for the preparation of $RuYO_{2-x}$/C.

Fig. S1). Subsequently, intermetallic RuY anchored on two-dimensional graphene was prepared by a one-pot solvothermal method. A mixed solution of $RuCl_3$ and H_xYO_{2-x} was then added to graphene to form $RuYO_{2-x}/C$ nanocomposites. The detailed structural model of $RuYO_{2-x}/C$ on the [222] planes was enlarged to determine the association and arrangement of atoms. The obtained $RuYO_{2-x}/C$ electrocatalyst with a small number of oxygen vacancies (V_o) exhibited desirable electrocatalytic properties. For the sake of comparison, we also utilized yttrium powder (Y) to synthesize the corresponding $RuYO_x/C$ directly, which might show the difference between the Y powder and the H_xYO_{2-x} bronzes (the $RuYO_{2-x}/C$ was prepared from Y powder, while the $RuYO_{2-x}/C$ was prepared from the as-prepared H_xYO_{2-x} bronze) from the same synthetic process.
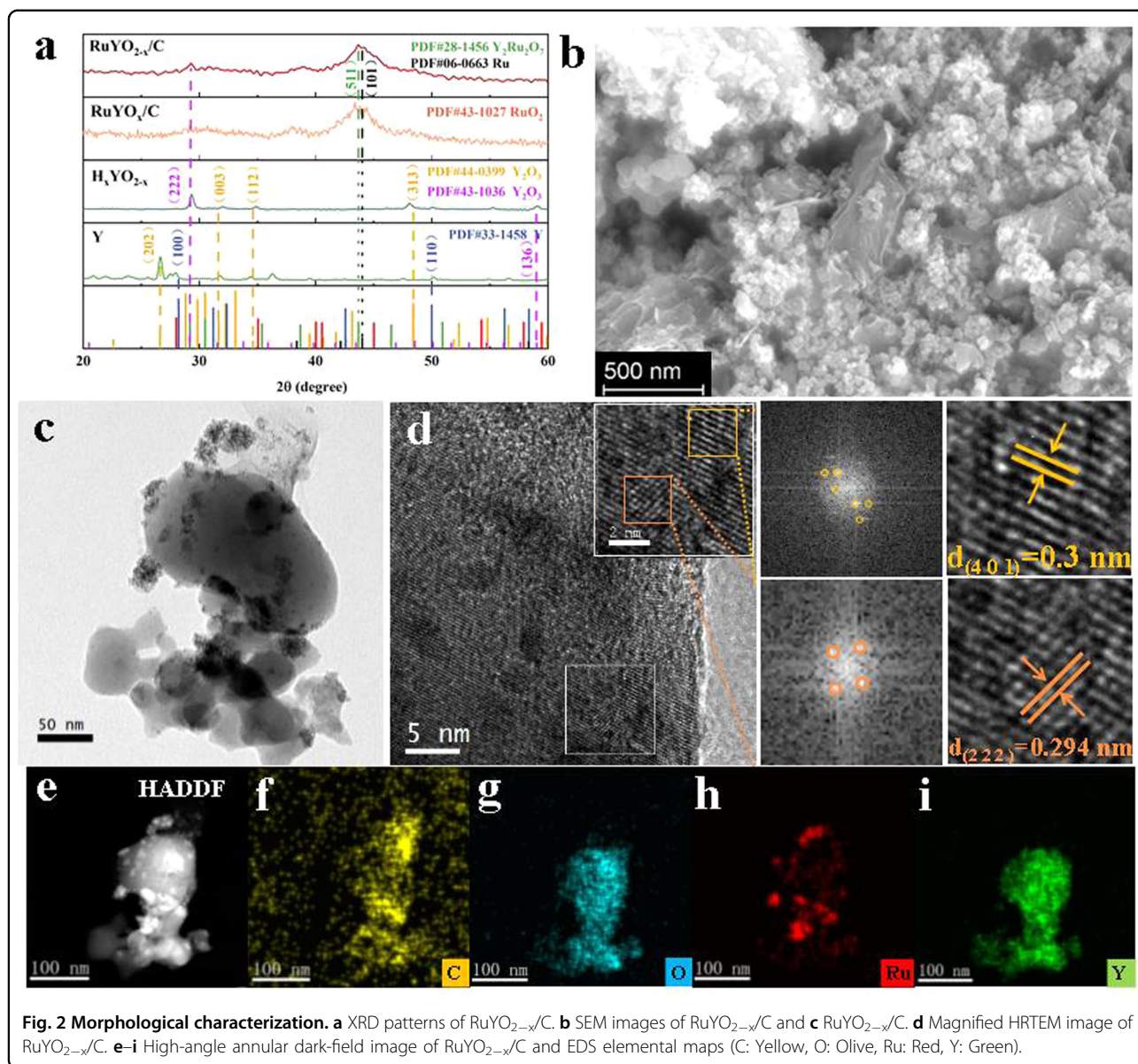
The crystal structures of the Y powder and the prepared H_xYO_{2-x}, $RuYO_{2-x}/C$, and $RuYO_x/C$ electrocatalysts were characterized by X-ray diffraction (XRD), as shown in Fig. 2a. The XRD patterns of the as-prepared materials showed their well-defined crystalline structures. The peaks for H_xYO_{2-x} appeared at 29.16°, 32°, 34.5°, 48.14°, and 59.09°, which were indexed to the (222), (003), (112), (313), and (136) lattice planes of Y_2O_3 (PDF#43–1036 and PDF#44–0399), respectively. There was also a peak for Y_2O_3 in the XRD pattern for the Y powder, probably because it was oxidized in air. Compared to those for the Y powder, the peaks for H_xYO_{2-x} were moved to higher angles, indicating lattice shrinkage, which might have been caused by oxygen vacancies. $RuYO_{2-x}/C$ and $RuYO_x/C$ had sharp peaks at 43.7° and 43.419°, respectively, which corresponded to the (511) lattice plane of $Y_2Ru_2O_7$ (PDF#28–1456) and indicated successful binding of Ru and Y. Compared with $RuYO_x/C$, the peak for $RuYO_{2-x}/C$ moved to a higher angle, indicating that the lattice of $RuYO_{2-x}/C$ shrank due to the presence of oxygen vacancies[41]. In addition, $RuYO_{2-x}/C$ showed a small peak at 29.19°, which was attributed to the (222) crystal face of Y_2O_3 (PDF#43–1036). To investigate whether RuO_2, as well as Ru, was formed in the $RuYO_{2-x}/C$, the standard data for RuO_2 (PDF#43–1027) and Ru (PDF#06–0663) were added to the XRD pattern. The results showed that there was no peak for RuO_2 in the $RuYO_{2-x}/C$ and $RuYO_x/C$, which might have been caused by the low content of RuO_2 formed via Ru oxidation. In $RuYO_{2-x}/C$ and $RuYO_x/C$, a small peak at 44.06° corresponded to the (101) lattice place of Ru, indicating the presence of a small amount of Ru.

Scanning electron microscopy (SEM) and transmission electron microscopy (TEM) measurements were used to probe the morphological characteristics. The surface morphologies of the $RuYO_{2-x}/C$ nanocomposites are shown in Fig. 2b and Supplementary Fig. S2a, b, which indicated that $RuYO_{2-x}/C$ was composed of densely packed particles grown onto the graphene sheets. Figure 2c and Supplementary Fig. S3 show the TEM images of $RuYO_{2-x}/C$, further demonstrating that the as-prepared nanomaterials were spherical particles loaded on graphene. To investigate the interior lattice, high-resolution TEM (HRTEM) images of $RuYO_{2-x}/C$ are shown in Fig. 2d and marked with yellow and orange rectangles. Figure 2d displays the HRTEM images of the $RuYO_{2-x}/C$ sample, which were accompanied by FFT patterns and IFFT patterns of the selected areas. From Supplementary Fig. S3c, d, 7 and 4 stripes were calculated, respectively. Finally, the lattice spacings of $RuYO_{2-x}/C$ were determined to be 0.3 nm and 2.94 nm, which corresponded to the (401) lattice planes of Y_2O_3 (PDF#44–0399; d = 2.992 Å) and the (222) lattice planes of $Ru_2Y_2O_7$ (PDF#28–1456; d = 2.929 Å), respectively. In addition, the lattice fringes of $RuYO_{2-x}/C$ at the edge were blurred, which might have been due to the formation of oxygen vacancies induced by hydrogen reduction[42]. The high-angle annular dark-field scanning transmission electron microscopy (HAADF-STEM) image in Fig. 2e–i revealed the distributions of O, Ru, and Y elements in the catalyst. Energy dispersive spectroscopy (EDS) spectroscopy showed that the atomic ratio of Y and Ru in the as-prepared $RuYO_{2-x}/C$ sample was 13.08:8.84 (Supplementary Fig. S2f), which corresponded to an approximate composition ratio of 0.12:0.88 shown for the Y and Ru in $RuYO_{2-x}/C$ by ICP-AES (Supplementary Tables S2 and S1). In addition, we captured TEM images of H_xYO_{2-x} with the same method, and Supplementary Fig. S4a shows that H_xYO_{2-x} formed multilayered stacked sheets, and the crystal plane spacing of H_xYO_{2-x} was 0.17 nm in the high-resolution HRTEM images (Supplementary Fig. S4b, c), corresponding to the (7 1–2) crystal faces of Y_2O_3 (PDF#44–0399). Supplementary Fig. S4d–f showed that Y and O were evenly distributed, and combined with the XRD analysis of H_xYO_{2-x}, it was clear that the Y powder had been oxidized to H_xYO_{2-x}. The atomic ratio of Y to O in the H_xYO_{2-x} was 67.66:32.34, as shown by the energy dispersive analysis (EDS) in Supplementary Fig. S4g.

Chemical valence states and band structures

X-ray photoelectron spectroscopy (XPS) was used to investigate the electronic structures and valence states of the $RuYO_{2-x}/C$ and $RuYO_x/C$ electrocatalysts and H_xYO_{2-x}. The XPS survey spectrum showed the presence of Ru, Y and O in $RuYO_{2-x}/C$ and $RuYO_x/C$ and Y and O in H_xYO_{2-x}, $RuYO_{2-x}/C$ and $RuYO_x/C$ (Supplementary Fig. S5). The atomic ratios of the elements in the $RuYO_{2-x}/C$ and $RuYO_x/C$ catalysts were estimated with XPS, as shown in Supplementary Table S2. The ratio of Ru/Y atoms measured with XPS (2.6:0.5) was much larger than that measured with EDS (8.84:13.08) because XPS only detected the surface atoms at depths of a few

Fig. 2 Morphological characterization. a XRD patterns of RuYO$_{2-x}$/C. **b** SEM images of RuYO$_{2-x}$/C and **c** RuYO$_{2-x}$/C. **d** Magnified HRTEM image of RuYO$_{2-x}$/C. **e–i** High-angle annular dark-field image of RuYO$_{2-x}$/C and EDS elemental maps (C: Yellow, O: Olive, Ru: Red, Y: Green).

nanometers, which revealed the presence of a Ru surface in RuYO$_{2-x}$/C[43]. The Ru 3d spectra of RuYO$_{2-x}$/C and RuYO$_x$/C are shown in Fig. 3a. In RuYO$_{2-x}$/C, the peaks at 280.1 eV and 284.4 eV were the Ru 3d$_{5/2}$ and Ru 3d$_{3/2}$ binding energies for Ru^0, and those at 281.18 eV and 286.1 eV were the Ru 3d$_{5/2}$ and Ru 3d$_{1/2}$ peaks for Ru^{4+}, respectively[42,44]. The four Ru 3d peaks seen for RuYO$_x$/C were roughly the same as those for RuYO$_{2-x}$/C (Ru^0: 280.1 eV and 284.4 eV; Ru^{4+}: 282.18 eV and 286.1 eV). The Ru 3p spectra for RuYO$_{2-x}$/C and RuYO$_x$/C are shown in Fig. 3b. The peaks at 461.8 eV and 483.43 eV for RuYO$_{2-x}$/C were attributed to the Ru 3p$_{5/2}$ and Ru 3p$_{3/2}$ states of Ru^0, confirming the presence of Ru^0. The peaks at 486 eV and 463.46 eV were those of Ru^{4+}, which might have been caused by oxidation[45]. The peak for Ru^0 in

RuYO$_x$/C was divided into peaks at 484.14 eV (Ru 3p$_{1/2}$) and 461.88 eV (Ru 3p$_{3/2}$), and the peaks at 463.66 eV and 487.14 eV were assigned to the 3p$_{3/2}$ and 3p$_{3/2}$ states of Ru^{4+}. The Ru 3p peaks for RuYO$_{2-x}$/C showed positive displacements compared with those for RuYO$_x$/C. Combined with the peak areas for RuYO$_{2-x}$/C and RuYO$_x$/C in Supplementary Table S3, the dominant species in RuYO$_x$/C was Ru^0. The Ru^0 reduced the dissociation energy of H$_2$O and optimized the free energy for hydrogen adsorption[46]. When Ru was bound to H$_x$YO$_{2-x}$, the ratio of Ru^{4+} to Ru^0 was increased, which meant that the ability of Ru to lose electrons was enhanced, and the valence state was increased.

As shown in Fig. 3c, we compared the Y 3d spectra for RuYO$_{2-x}$/C, RuYO$_x$/C and H$_x$YO$_{2-x}$. Two peaks at
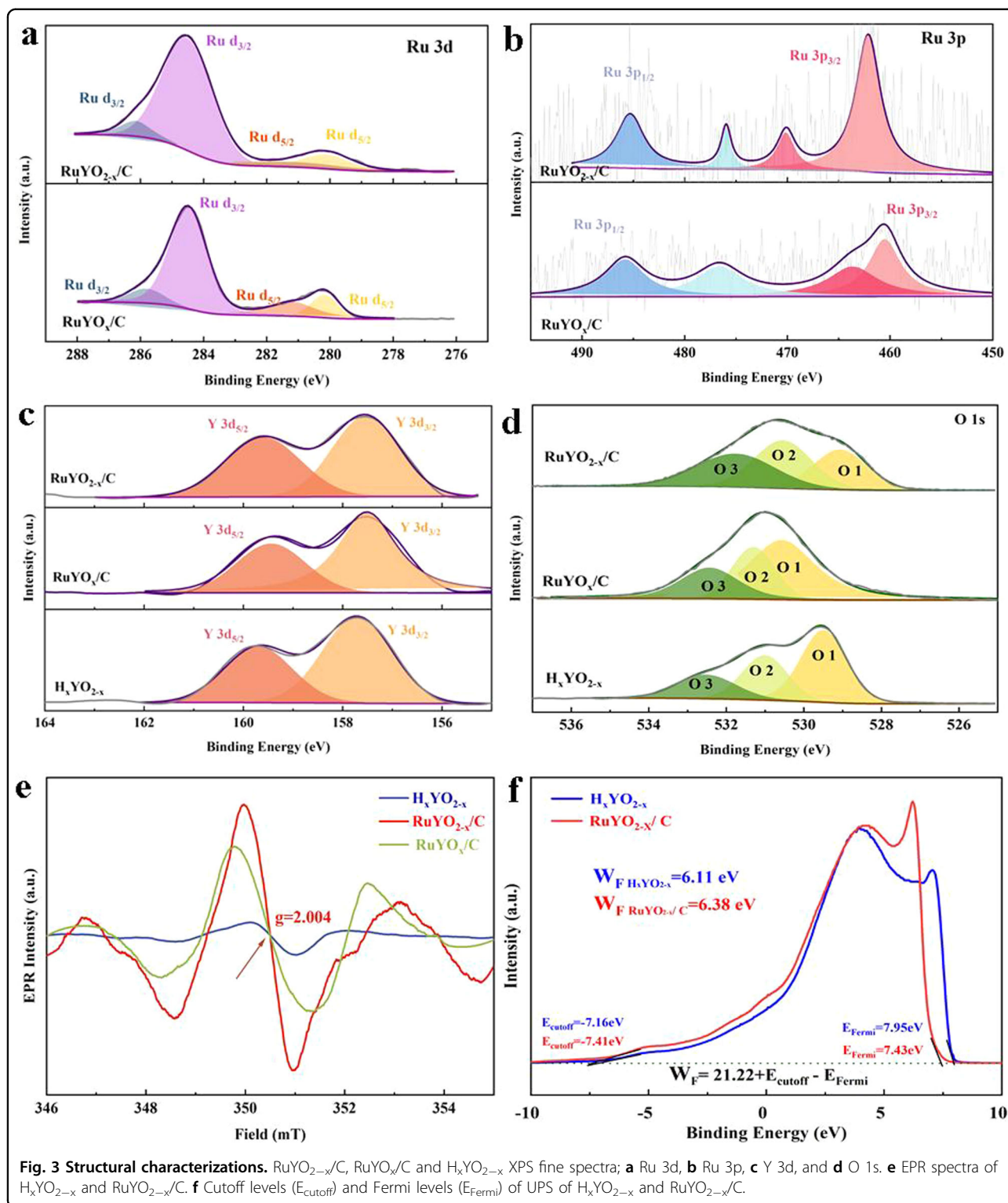
Fig. 3 Structural characterizations. $RuYO_{2-x}/C$, $RuYO_x/C$ and H_xYO_{2-x} XPS fine spectra; **a** Ru 3d, **b** Ru 3p, **c** Y 3d, and **d** O 1s. **e** EPR spectra of H_xYO_{2-x} and $RuYO_{2-x}/C$. **f** Cutoff levels (E_{cutoff}) and Fermi levels (E_{Fermi}) of UPS of H_xYO_{2-x} and $RuYO_{2-x}/C$.

157.5 eV and 159.43 eV for $RuYO_x/C$ were attributed to the Y $3d_{5/2}$ and Y $3d_{3/2}$ states, respectively; compared to those for $RuYO_{2-x}/C$ (Y $3d_{5/2}$: 157.53 eV; Y $3d_{3/2}$: 159.6 eV) and H_xYO_{2-x} (Y $3d_{5/2}$: 157.7 eV; Y $3d_{3/2}$: 159.7 eV), the peaks for $RuYO_x/C$ had obvious negative displacements, indicating that the extents of Y oxidation in $RuYO_{2-x}/C$ and H_xYO_{2-x} were higher than that in $RuYO_x/C$[47]. Compared with those for H_xYO_{2-x}, the Y 3d states for $RuYO_{2-x}/C$ exhibited lower binding energies, revealing that electron accumulation in Y optimized the

hydrogen adsorption process. Combined with the XPS results for Ru, this showed that some electrons in Ru were transferred to Y, and doping with Ru adjusted the interfacial electronic structure of the catalyst. The Ru and Y synergistically improved the catalytic performance.

Oxygen vacancies (V_o) are common in metal oxides, and they often enhance surface electrocatalysis and promote electron transfer[41]. In general, the O 1s XPS peaks could be divided into three regions for metal-O, V_o, and adsorbed water molecules[48,49]. The O 1s XPS spectra of $RuYO_{2-x}/C$, $RuYO_x/C$, and H_xYO_{2-x} are shown in Fig. 3d ($RuYO_{2-x}/C$ (Ru/Y-O: 529 eV; V_o: 530.53 eV; adsorbed water molecules: 531.7 eV)), $RuYO_x/C$ (Ru/Y-O: 531.36 eV; V_o: 531 eV; adsorbed water molecules: 533 eV) and H_xYO_{2-x} (Y-O: 529.48 eV; V_o: 531 eV; adsorbed water molecules: 532.52 eV). It is worth noting that the proportion of V_o peak area in $RuYO_{2-x}/C$ was 37.06%, which was higher than those in $RuYO_x/C$ (23.81%) and H_xYO_{2-x} (21.13%) (Supplementary Table S4), indicating that there were abundant oxygen vacancies in $RuYO_{2-x}/C$[50]. The low V_o peak area ratio of H_xYO_{2-x} revealed that the electronic interactions between Ru and Y were the main reason for the oxygen vacancies in the $RuYO_{2-x}/C$ catalyst. Electron transfer from Ru to Y led to a decrease in the metal-O content, which led to oxygen escape and more oxygen vacancies in $RuYO_{2-x}/C$[51].
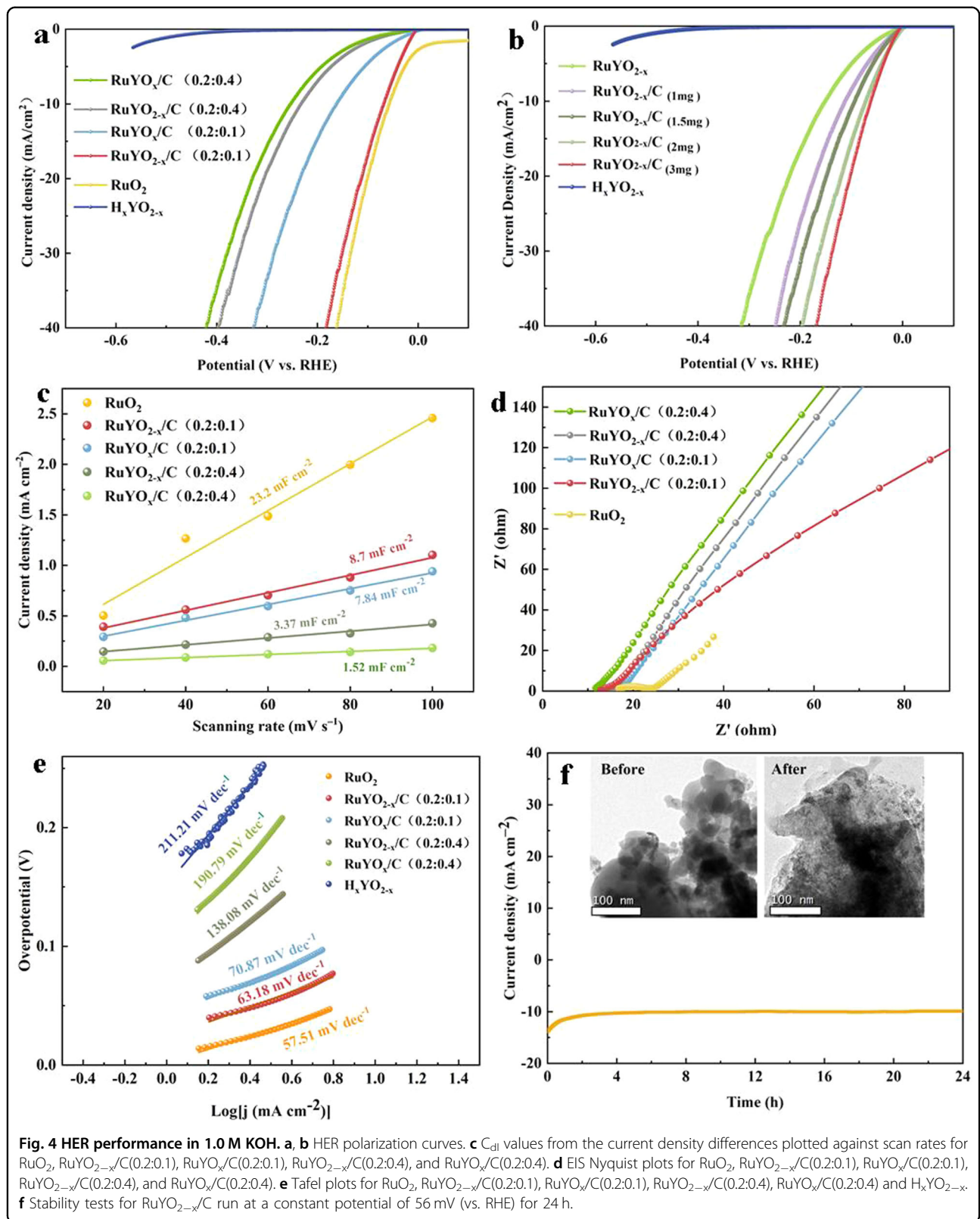
Electron paramagnetic resonance (EPR) measurements confirmed the formation of oxygen vacancies in $RuYO_{2-x}/C$, as shown in Fig. 3e. As expected, the Ru cations were stabilized by the oxygen vacancies, which was attributed to an electronic coupling mechanism[52]. $RuYO_{2-x}/C$, $RuYO_x/C$, and H_xYO_{2-x} all exhibited symmetric EPR peaks at g = 2.004, which were caused by unpaired electrons at the oxygen vacancies[53]. The EPR signal strength was related to the number of oxygen vacancies, and the higher signal strength of the $RuYO_{2-x}/C$ adhesive indicated that there were abundant oxygen vacancies in the $RuYO_{2-x}/C$ catalyst, which was consistent with the results of the XPS analyses. After Ru was combined with H_xYO_{2-x}, the electronic structure changed and the lattice distortion caused by the oxygen vacancies increased the conductivity of the catalyst, facilitated the adsorption of H_2O and OH^- groups on the surface of the catalyst and improved the electrocatalytic performance[54–56].

In addition, to confirm the preparation of the catalytic materials via electron escape, ultraviolet photoelectron spectroscopy (UPS) studies and work function (W_F) calculations were performed for H_xYO_{2-x} and $RuYO_{2-x}/C$ to determine the electron modulation mechanisms. As shown in Fig. 3f, the UPS results showed that the secondary electronic cutoff edges of the catalytic materials were closely related to the doping levels of Ru and Y[57]. The W_F is usually approximately half the ionization energy of a metal-free atom. The W_F of a metal is

expressed as the minimum energy required for an electron with an initial energy equal to the Fermi level (E_F) to escape from the interior of the metal into a vacuum[58]. The value of the W_F is related to the surface condition, and the W_F also shows periodic changes as the atomic number increases. In semiconductors, the conduction band's minimum energy and the valence band's maximum energy are generally lower than the minimum electron escape energy of the metal. For an electron to escape from a semiconductor, it requires the corresponding amount of energy. This indicated that the E_F of the catalyst in this study was related to metal doping[59]. The value of E_F indicates how strongly the electrons are bound to the metal. A smaller E_F means it is easier for electrons to leave the metal[60,61]. The W_F value can be calculated from the formula in Fig. 3f. The slope of the VB-XPS plot shown in Supplementary Fig. S6a, b showed that the valence band maximum (VBM) values of H_xYO_{2-x} and $RuYO_{2-x}/C$ were −0.92 eV. The band diagram parameters calculated from the UPS data, including the vacuum level (E_{Vac}), E_F and the valence band (VB), are shown in Fig. 3f. H_xYO_{2-x} (E_F = 7.95 eV, W_F = 6.11 eV) had a higher E_f energy level and a lower W_F than $RuYO_{2-x}/C$ (E_F = 7.43 eV, W_F = 6.38 eV). This indicated that H_xYO_{2-x} had better electrical conductivity and could transfer electrons to $RuYO_{2-x}/C$[62]. After compounding with Ru atoms, $RuYO_{2-x}/C$ presented a higher W_F, which indicated a greater ability to resist electron loss and withstand the anode potential, which increased the positive working potential[63]. The UPS spectra of $RuYO_{2-x}/C$ with different graphene contents and the corresponding VB-XPS spectra of $RuYO_{2-x}$ are shown in Supplementary Fig. S6c, d.

HER electrocatalytic performance analyses

$RuYO_{2-x}/C$ exhibited electrical conductivity and oxygen vacancies. We investigated the HER catalytic capabilities of the synthesized catalysts in a typical three-electrode system with a 1.0 M KOH solution used as the electrolyte. For comparison, a commercial RuO_2 catalyst was tested as a reference. All potentials were referenced to that of the reversible hydrogen electrode (RHE). Figure 4a shows the linear scanning voltammetry (LSV) curves for the $Ru-YO_{2-x}/C$ and $Ru-YO_x/C$ series synthesized from H_xYO_{2-x} and yttrium powder with different ratios. Undoubtedly, commercial RuO_2 exhibited the highest catalytic activity, with an overpotential η_{10} = 46 mV at a current density of 10 mA cm^{-2}. Impressively, $RuYO_{2-x}/C(0.2:0.1)$ had an η_{10} of only 56 mV, indicating excellent electrocatalytic performance and an overpotential that was only 10 mV higher than that of RuO_2. The measured η_{10} values were 166 mV ($RuYO_x/C(0.2:0.1)$), 226 mV ($RuYO_{2-x}/C(0.2:0.4)$), and 246 mV ($RuYO_x/C(0.2:0.4)$). H_xYO_{2-x} showed almost no HER catalytic performance. As shown in Supplementary Fig. S7, an appropriate Ru/Y molar ratio slightly affected the catalytic

Fig. 4 HER performance in 1.0 M KOH. a, **b** HER polarization curves. **c** C_{dl} values from the current density differences plotted against scan rates for RuO_2, $RuYO_{2-x}/C(0.2:0.1)$, $RuYO_x/C(0.2:0.1)$, $RuYO_{2-x}/C(0.2:0.4)$, and $RuYO_x/C(0.2:0.4)$. **d** EIS Nyquist plots for RuO_2, $RuYO_{2-x}/C(0.2:0.1)$, $RuYO_x/C(0.2:0.1)$, $RuYO_{2-x}/C(0.2:0.4)$, and $RuYO_x/C(0.2:0.4)$. **e** Tafel plots for RuO_2, $RuYO_{2-x}/C(0.2:0.1)$, $RuYO_x/C(0.2:0.1)$, $RuYO_{2-x}/C(0.2:0.4)$, $RuYO_x/C(0.2:0.4)$ and H_xYO_{2-x}. **f** Stability tests for $RuYO_{2-x}/C$ run at a constant potential of 56 mV (vs. RHE) for 24 h.

performance of the prepared $RuYO_{2-x}/C$ and $RuYO_x/C$ in the HER. The LSV results revealed that with increasing Y concentration, the performance of the synthesized catalyst decreased, which might have occurred because trace Y coordinated and cooperated with the Ru to improve the catalytic performance. Under the same conditions, we also compared the electrocatalytic performance of $RuYO_{2-x}/C(0.2:0.1)$ with different graphene contents (Fig. 4b). The HER performance of $RuYO_{2-x}/C$ with a 3 mg graphene content (0.2:0.1) still showed excellent electrochemical activity, while the catalytic activity of $RuYO_{2-x}$ with 0 mg graphene content was minimal (146 mV). Previous studies showed that most electrocatalysts are prone to corrosion and passivation in extreme environments. Due to the surface corrosion resistance and excellent electrical conductivities of carbon materials, the electrocatalytic activities and stabilities of metal nanoparticles are effectively enhanced after coupling with carbon[64,65]. The overpotentials for other $RuYO_{2-x}/C(0.2:0.1)$ catalysts with different graphene contents were 116 mV ($RuYO_{2-x}/C$ (1 mg)), 86 mV ($RuYO_{2-x}/C$ (1.5 mg)), and 66 mV ($RuYO_{2-x}/C$ (1 mg)).

The electrochemically active surface area (ECSA) is a significant parameter revealing the intrinsic electrocatalytic activity of a catalyst, and it is determined from the double-layer capacitance (C_{dl}) measured with cyclic voltammetry (CV)[66]. The electrochemical active surface area (ECSA) was estimated based on $ECSA = C_{dl}/C_s$, where C_{dl} corresponds to the double-layer charging current versus the scan rate and C_s corresponds to a specific capacitance[67]. To probe the electrocatalytic activity of $RuYO_{2-x}/C(0.2:0.1)$ in more depth, we calculated the electrochemically active surface area (ECSA) by measuring the C_{dl} values from the CV curves (Fig. 4c). The C_{dl} value for $RuYO_{2-x}/C(0.2:0.1)$ was 8.7 mF cm^{-2}, which was higher than those of $RuYO_x/C(0.2:0.1)$ (7.84 mF cm^{-2}), $RuYO_{2-x}/C(0.2:0.4)$ (3.37 mF cm^{-2}), and $RuYO_x/C(0.2:0.4)$ (1.52 mF cm^{-2}), which indicated that the $RuYO_{2-x}/C(0.2:0.1)$ electrode had more active sites. The C_{dl} values of $RuYO_{2-x}/C(0.2:0.1)$ with different graphene contents are shown in Supplementary Fig. S9 and Fig. 9. Electrochemical impedance spectroscopy (EIS) was also employed to investigate the HER kinetics. The impedance spectrum (Fig. 4d, Supplementary Fig. S10) showed that the charge transfer resistance of the $RuYO_{2-x}/C(0.2:0.1)$ catalyst was the smallest among all of the materials, thus indicating that the $RuYO_{2-x}/C(0.2:0.1)$ electrode exhibited faster HER kinetics and accelerated faradaic processes. A Tafel slope analysis was carried out to investigate the reaction kinetics of the HER. As shown in Fig. 4e and Supplementary Fig. S11, $RuYO_{2-x}/C(0.2:0.1)$ exhibited an apparently low Tafel slope of 63.18 mV dec^{-1}, which corresponded to Tafel step-limited HER kinetics. A linear fit for the Tafel data showed that the Tafel slope for $RuYO_{2-x}/C(0.2:0.1)$ was only 5.67 mV

dec^{-1} higher than that for RuO_2, and $RuYO_{2-x}/C(0.2:0.1)$ exhibited the most efficient HER reaction kinetics among the other synthesized materials. Figure 4f indicates that no significant current decay was observed after 24 h of continuous $RuYO_{2-x}/C(0.2:0.1)$ testing with a current density of 10 mA cm^{-2}. We performed TEM tests on the $RuYO_{2-x}/C(0.2:0.1)$ catalysts before and after HER electrocatalysis. The chronoamperometry curve shown in Fig. 4f for $RuYO_{2-x}/C(0.2:0.1)$ indicated that the current density was maintained with negligible loss during a 24 h stability test, which revealed the excellent long-term electrochemical stability of $RuYO_{2-x}/C(0.2:0.1)$. The stability of the morphology was the main reason for the stable performance of the $RuYO_{2-x}/C(0.2:0.1)$ catalysts. The inset in Fig. 4f displays HRTEM images of the $RuYO_{2-x}/C(0.2:0.1)$ sample after stability testing, which was accompanied by the FFT patterns and IFFT patterns of the selected areas in Supplementary Fig. S12b. Supplementary Fig. S12c reveals that the lattice fringe spacing was 0.301 nm, which corresponded to the (401) crystal surface of Y_2O_3. The distributions of elements in $RuYO_{2-x}/C(0.2:0.1)$ after the stability test are shown in Supplementary Fig. S12d, i. The composition and distributions of the elements in $RuYO_{2-x}/C(0.2:0.1)$ barely changed after the stability test. In addition, we determined the effects of different loadings of $RuYO_{2-x}/C(0.2:0.1)$ catalyst inks on the glassy carbon electrode. The best HER performance of 56 mV was reached when the ink concentration on the glassy carbon electrode was 0.42 µg cm^{-2}. As shown in Supplementary Fig. S13, the HER performance gradually stabilized as the catalyst load on the glassy carbon electrode was increased. Supplementary Fig. S14 shows photographs of the nickel foam used for stability testing. A comprehensive consideration of the hydrogen evolution potential, Tafel slope, electric double-layer capacitance, and impedance of $RuYO_{2-x}/C(0.2:0.1)$ indicated that the nanomaterials constructed from Ru, Y and graphene accelerated charge transfer and thus improved the hydrogen evolution performance of the materials. Subsequently, as shown in Table 1[46,47,68–75], we also compared the performance with those of other reported electrocatalysts, and the performance of our synthesized $RuYO_{2-x}/C$ catalyst was superior. First, the capacities of Ru-based catalysts to bind hydrogen are similar to those of Pt, and they have excellent catalytic ability for the HER. Although it is also a precious metal, Ru is relatively inexpensive and more abundant than Pt, making it the most promising substitute for Pt. We combined Ru with the rare earth element Y. Because Y itself has good electrical conductivity and a smaller ionic radius than Ru, it formed oxygen vacancies and changed the structure. In addition, the EDS and XPS quantitative analyses showed that the contents of Ru in the $RuYO_{2-x}/C$ catalysts were low, and appropriate proportions of Ru

Table 1 Comparison of reported electrocatalysts on basic HER activity.

Catalyst	Electrolyte	Tafel slope/ mV dec $^{-1}$	Overpotential at 10 mA cm $^{-2}$ /mV
RuYO$_{2-x}$/C	**1 M KOH**	**63.18**	**56**
NiY-MOF/NF	1 M KOH	80	136
RuNi-Alloy@SC	1 M KOH	96	93
RuFe@NF	1 M KOH	63.39	28
Pd-Ru@NG	1 M KOH	42	42
Ru-G/CC	1 M KOH	76	40
Ru / CoO	1 M KOH	70	55
SA-Ru-MoS$_2$	1 M KOH	21	76
Ru black	1 M NaOH	80	125
RuNi-0 NPNWs	1 M KOH	69	129

The bold values show this study's data.

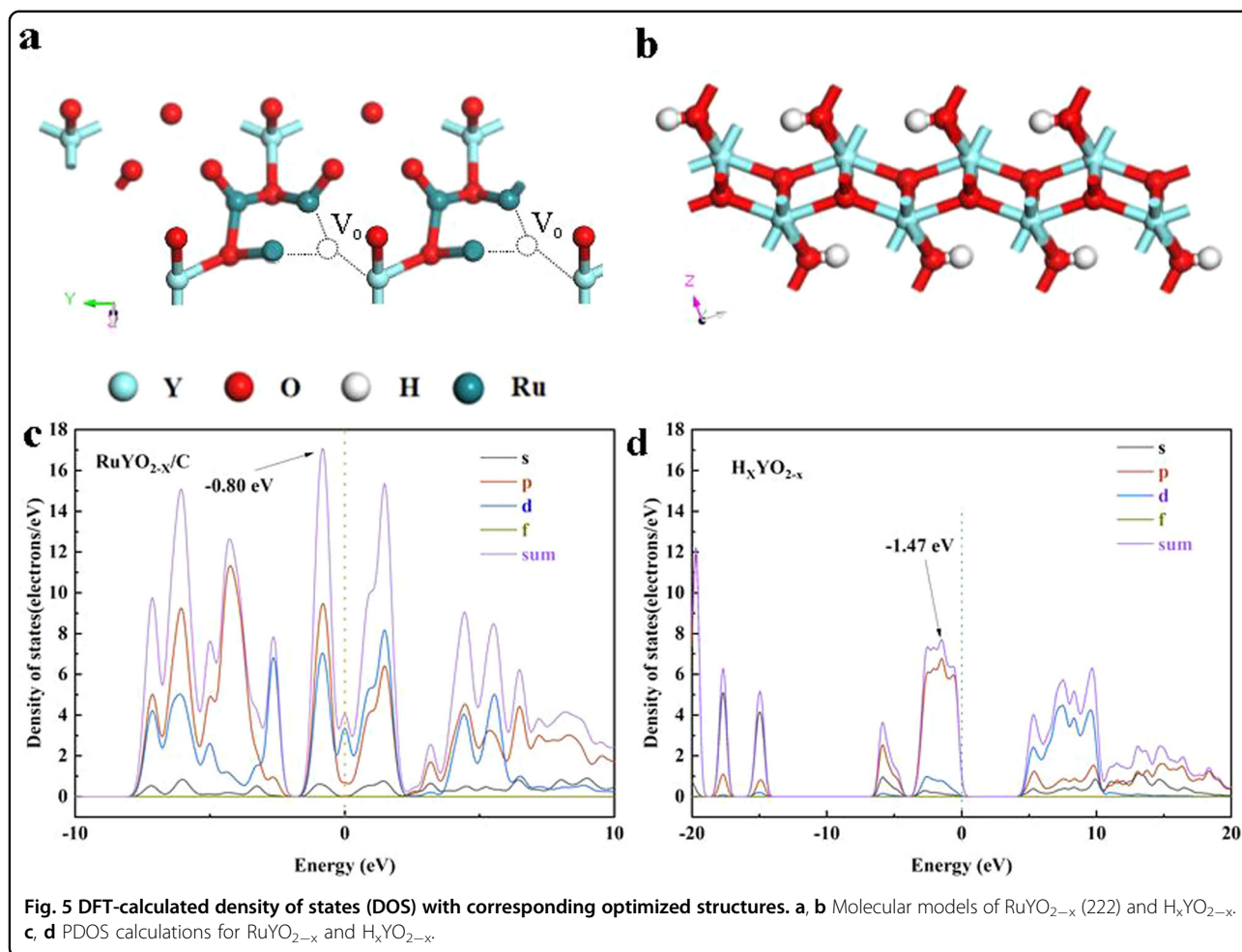and Y synergistically enhanced the electrocatalytic activity, so RuYO$_{2-x}$/C exhibited excellent HER catalysis.

Electrocatalytic enhancement mechanism

The alkaline HER follows the Volmer-Heyrovsky or Volmer-Tafel mechanistic pathways (Volmer: $H_2O + M + e^- \rightarrow M\text{-}H^* + OH^-$; Heyrovsky: $H_2O + M\text{-}H^* + e^- \rightarrow H_2 + OH^- + M$; Tafel: $2\ M\text{-}H^* \rightarrow H_2 + 2\ M$). To gain more insight into the excellent electrocatalytic hydrogen evolution performance of RuYO$_{2-x}$/C in alkaline media, we simulated the RuYO$_{2-x}$ bimetallic nanoparticles and H$_x$YO$_{2-x}$ to determine their effects on the electronic structure at the atomic level (Fig. 5a, b)[76]. Herein, we selected the (222) surface of RuYO$_{2-x}$/C and the corresponding TEM and XRD results. A highly active catalyst enabling hydrogen production from water splitting effectively promotes hydrogen release and hydrogen adsorption. The E_F value of H$_x$YO$_{2-x}$ was much larger than that of RuYO$_{2-x}$ after the combination of Ru and H$_x$YO$_{2-x}$. This indicated that electron transfer occurred during the combination of Ru and H$_x$YO$_{2-x}$, thus improving the HER performance[77]. In alkaline media, the overall HER reaction pathway includes the dissociation of H$_2$O and the formation of adsorbed hydrogen intermediates, as well as ultimate hydrogen generation[78–80]. Therefore, superior alkaline HER electrocatalysts should simultaneously exhibit moderate H binding energy and a relatively low H$_2$O dissociation barrier. Figure 5c, d displays the H adsorption energies (ΔE_H) calculated for the RuYO$_{2-x}$ and H$_x$YO$_{2-x}$ surfaces, and the corresponding H adsorption structures are shown in Supplementary Fig. S15. Subsequently, we also calculated the hydrogen adsorption free energies (ΔG_{H^*}) for RuYO$_{2-x}$ (222) and H$_x$YO$_{2-x}$ to evaluate their HER activities; higher ΔG_{H^*}

values indicate weaker hydrogen adsorption, and vice versa[81]. From a thermodynamic perspective, the ideal Gibbs free energy for the adsorbed hydrogen atoms should be close to zero[82].

An electron density difference (EDD) analysis (Fig. 6a, b) revealed the electronic structure of RuYO$_{2-x}$ and confirmed that the Y sites had accumulated electron density, while the Ru centers lost electron density and were considered to be the superior activation sites for OH adsorption, which was consistent with the XPS data. Hydrogen adsorption was extremely weak on the external surfaces of H$_x$YO$_{2-x}$, but it was much stronger on the inner surfaces, suggesting that the interior of H$_x$YO$_{2-x}$ was more favorable for hydrogen adsorption. In conjunction with the previous UPS analysis, a reasonable explanation for hydrogen spillover from H$_x$YO$_{2-x}$ to Ru is as follows: the difference in W_F values for RuYO$_{2-x}$ and H$_x$YO$_{2-x}$ led to electron accumulation at the subsurface of H$_x$YO$_{2-x}$, which enhanced hydrogen adsorption and moved internal protons to the external surface. The Gibbs free energy for adsorption at standard atmospheric pressure (G_{ads}) was defined as $G_{ads} = E_{ads} + \Delta G(T)$, where $\Delta G(T)$ is the sum of Gibbs free energy corrections at temperature T. Hence, we concluded that $\Delta G(T) = \Delta ZPE + \Delta H(T) - T\Delta S(T)$, where ZPE, $\Delta H(T)$, and $\Delta S(T)$ represented the zero-vibration energy change, the enthalpy change, and the entropy change after adsorption. Figure 6c and Supplementary Fig. S16 indicate that the ΔG_{H^*} of RuYO$_{2-x}$ was closer to the optimal value for the HER ($\Delta G_{H^*} = 0$ eV) than those of the other substrates, which supported the experimental results indicating that RuYO$_{2-x}$ showed better HER activity than H$_x$YO$_{2-x}$. Overall, the RuYO$_{2-x}$ catalyst with more Ru-O-Y bonds and V$_O$ significantly reduced the energy barrier for breaking the H-OH bonds and accelerated water dissociation. In addition, the strong metal-support interactions resulted in the optimum energy for hydrogen adsorption and desorption. These phenomena synergistically rationalized the enhanced activity and favorable kinetics seen for RuYO$_{2-x}$ in catalytic hydrogen evolution in alkaline electrolytes. The combination of Ru and H$_x$YO$_{2-x}$ was a key factor determining the HER activity.

A mechanism was proposed to explain the greatly enhanced HER activity of RuYO$_{2-x}$/C in alkaline media. Under an applied cathodic potential, protons in the electrolyte were inserted into the oxygen-deficient H$_x$YO$_{2-x}$ and then combined with Ru on a graphene substrate to produce RuYO$_{2-x}$/C. The abundance of oxygen vacancies in RuYO$_{2-x}$/C markedly increased the proton storage capacity and enhanced charge transfer. As a result, the oxygen-deficient H$_x$YO$_{2-x}$ acted as a proton reservoir to supply protons to the Ru surface, which recombined to evolve molecular hydrogen. As the overpotentials were increased, the H$_x$YO$_{2-x}$ dissociated water to generate protons, which also spilled over to Ru. The hydrogen spillover from the H$_x$YO$_{2-x}$ to Ru

Fig. 5 DFT-calculated density of states (DOS) with corresponding optimized structures. a, b Molecular models of $RuYO_{2-x}$ (222) and H_xYO_{2-x}. **c, d** PDOS calculations for $RuYO_{2-x}$ and H_xYO_{2-x}.

changed the rate-limiting step of the HER on Ru in a neutral alkaline solution from water dissociation to hydrogen recombination, which greatly improved the HER kinetics.

Conclusions

In summary, we designed a high-density $RuYO_{2-x}/C$ bimetallic nanocomposite with low Ru loadings and grown on two-dimensional graphene sheets. The interactions between the Ru atoms and H_xYO_{2-x} were key to the catalytic performance of $RuYO_{2-x}/C$ in hydrogen production via hydrolysis. To demonstrate the high catalytic activity of Ru combined with H_xYO_{2-x}, a number of $RuYO_x/C$ catalysts with Ru atoms combined with yttrium monomers were also prepared for comparison. Additionally, the presence of V_o was crucial in promoting the hydrogen evolution reaction. With the same ratio of bimetallic atoms, it is noteworthy that $RuYO_{2-x}/C$ exhibited high HER activity in alkaline media as well as long-term stability. Therefore, $RuYO_{2-x}/C$ exhibits potential for application as a water-splitting catalyst.

Methods

Materials

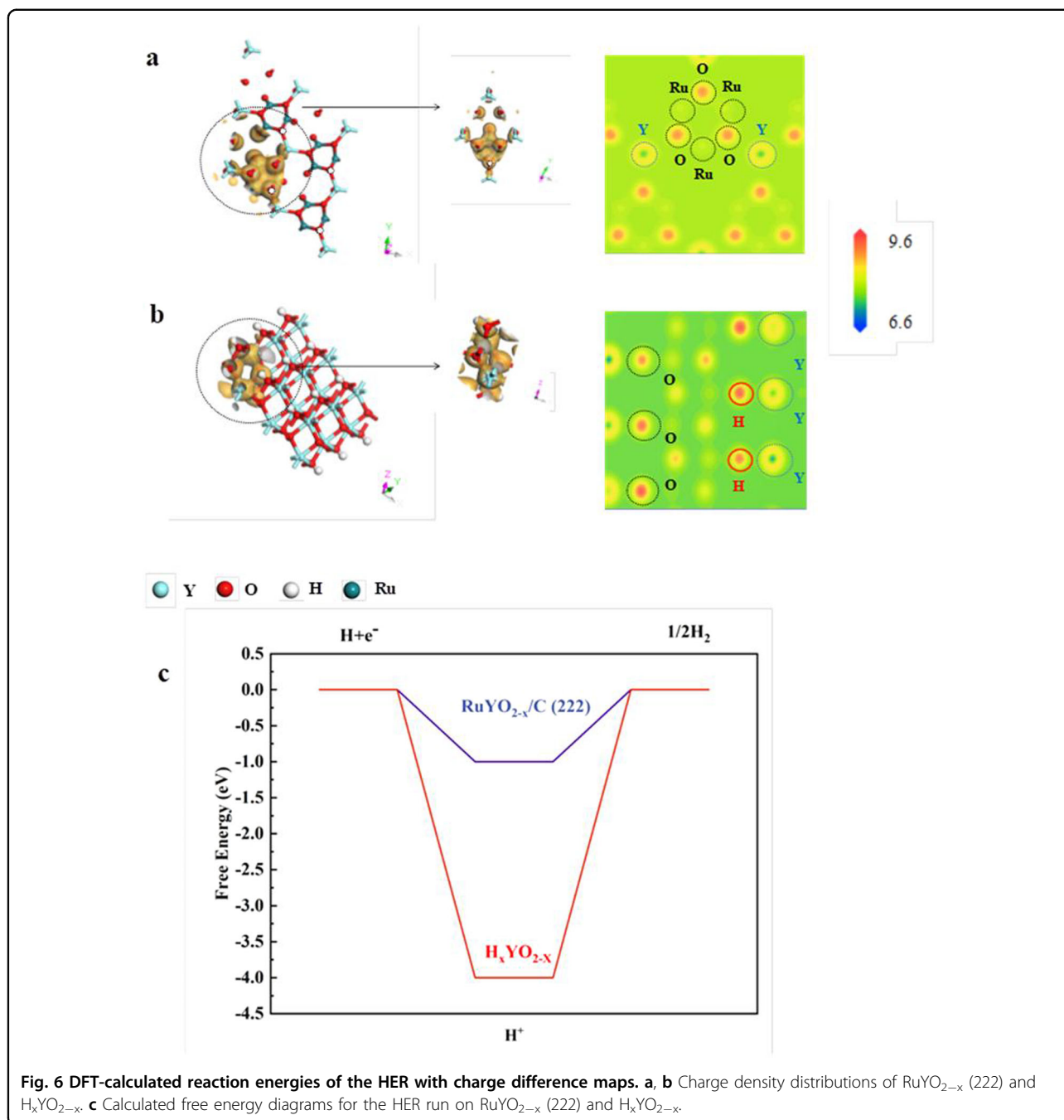Ruthenium(III) trichloride hydrate ($RuCl_3 \cdot xH_2O$, 99%), yttrium (Y, 99.9%) graphene (C, >95%), N,N-dimethyl-formamide (DMF, 99.5%), Nafion solution (5wt.%, contain 15–20% water), potassium hydroxide (KOH, 90%) and ethanol (C_2H_5OH, 99.9%) were purchased from Aladin Reagent. Hydrogen peroxide (H_2O_2, ≥30% reagent) was purchased from Greagent. All materials were used directly without any purification. The 18 MΩ cm^{-1} deionized water was prepared with an ultra-pure purifying device.

Synthesis of H_xYO_{2-x}

Yttrium power, 0.1 g, was weighed and added to 10 mL of anhydrous ethanol, then 0.4 mL of hydrogen peroxide solution was added to the mixed solution with a pipette; the solution was stirred vigorously for 18 h, placed into an oven at 60 °C to dry for 1 h and then removed.

Synthesis of $Ru-YO_{2-x}/C$

First, 3 mg of graphene was weighed into a centrifuge tube with 10 mL of deionized water. Then, 1 mL of

Fig. 6 DFT-calculated reaction energies of the HER with charge difference maps. a, b Charge density distributions of $RuYO_{2-x}$ (222) and H_xYO_{2-x}. **c** Calculated free energy diagrams for the HER run on $RuYO_{2-x}$ (222) and H_xYO_{2-x}.

anhydrous ethanol and DMF was added, and the mixture was sonicated for 30 min. $RuCl_3 \cdot xH_2O$ (0.2 mmol) and H_xYO_{2-x} (0.1 mmol) were added to the sonicated graphene mixture and sonicated for 30 min.

The mixed liquid was transferred to a 20 mL stainless steel autoclave in a PTFE-lined bottle and placed in an oven at 120 °C for 16 h. After the reaction was completed and the autoclave had cooled naturally to room temperature, the product was washed by centrifugation with anhydrous ethanol three times and placed in an oven at

60 °C until the product was completely dry. The product was removed and ground to powder.

The Ru:Y molar ratios for the $Ru\text{-}YO_{2-x}/C$ catalysts prepared in this study were 0.2:0.1, 0.2:0.2, and 0.2:0.4.

Synthesis of Ru-YO$_x$/C

The $Ru\text{-}YO_x/C$ catalysts were prepared in the same way as the $Ru\text{-}YO_{2-x}/C$ catalysts, except that the H_xYO_{2-x} was replaced with Y powder.

Preparation of the supported catalysts

Four milligrams of catalyst was weighed into a centrifuge tube, and then 30 μL of Nafion solution and 1 mL of a mixture of water and ethanol (3:1) were added. The tube was sonicated for 40 min, and then 14 μL of liquid was dripped onto a glassy carbon electrode with an area of 0.196 cm^2 and allowed to dry naturally until a film was formed on the electrode surface.

Electrochemical measurements

The electrochemical properties of the materials was tested in 1.0 mol L^{-1} KOH solutions at room temperature with an electrochemical workstation (CHI760E). The working electrode was prepared by depositing the catalyst on a glassy carbon (GC) electrode with an area of 0.19625 cm^2. A saturated calomel electrode (SCE) and platinum flake electrode were utilized as the reference electrode and counter electrode, respectively. The polarization curves were acquired from linear sweep voltammetry (LSV) at a sweep rate of 5 mV·s^{-1}. The LSV curve was plotted as the logarithm of the standard potential and current density to obtain the Tafel diagram. Electrochemical impedance spectroscopy (EIS) was tested from 100 kHz to 1 Hz. The electrochemical double-layer capacitance (C_{dl}) was determined by cyclic voltammetry (CV), and the potential scan rates were 20, 40, 60, 80 and 100 mV·s^{-1}. The measured potentials vs. SCE were referenced to the reversible hydrogen electrode (RHE) with the following equation:

$$E(RHE) = E(SCE) + 0.231 + 0.0591pH \tag{1}$$

Author details
^{1}School of Chemical and Environmental Engineering, Shanghai Institute of Technology, 201418 Shanghai, China. ^{2}State Key Laboratory for Modification of Chemical Fibers and Polymer Materials, College of Textile, Donghua University, 201620 Shanghai, China. ^{3}Key Laboratory of Optoelectronic Chemical Materials and Devices, School of Chemical and Environmental Engineering, Jianghan University, 430056 Wuhan, China

Author contributions
F.J. conceived the project and revised the manuscript. W.D. synthesized the material and conducted the TEM results. X.L. analyzed the XPS data. Y.W. conducted the SEM results. J.Z. analyzed the electrocatalytic performances. H.M. conducted the electrocatalytic results. T.L. analyzed the UPS and EPR data. R.Y. conducted DFT calculations. W.Z. revised the XRD results and analyzed the DFT calculations. All authors cowrote the manuscript.

Conflict of interest
The authors declare no competing interests.

Publisher's note
Springer Nature remains neutral with regard to jurisdictional claims in published maps and institutional affiliations.

Supplementary information The online version contains supplementary material available at https://doi.org/10.1038/s41427-023-00501-z.

References
1. Xu, J. et al. Frenkel-defected monolayer MoS$_2$ catalysts for efficient hydrogen evolution. *Nat. Commun.* **13**, 2193 (2022).
2. Zhang, J. et al. OH spectator at IrMo intermetallic narrowing activity gap between alkaline and acidic hydrogen evolution reaction. *Nat. Commun.* **13**, 5497 (2022).
3. Kumar, M., Meena, B., Subramanyam, P., Suryakala, D. & Subrahmanyam, C. Recent trends in photoelectrochemical water splitting: the role of cocatalysts. *NPG Asia Mater.* **14**, 88 (2022).
4. Yu, J. et al. Sustainable oxygen evolution electrocatalysis in aqueous 1 M H$_2$SO$_4$ with earth abundant nanostructured Co$_3$O$_4$. *Nat. Commun.* **13**, 4341 (2022).
5. Liang, Y. et al. Enhancement of electrocatalytic oxygen evolution by chiral molecular functionalization of hybrid 2D electrodes. *Nat. Commun.* **13**, 3356 (2022).
6. Wang, D., Sheng, T., Chen, J., Wang, H.-F. & Hu, P. Identifying the key obstacle in photocatalytic oxygen evolution on rutile TiO$_2$. *Nat. Catal.* **1**, 291–299 (2018).
7. Fu, Q. et al. Phase-junction electrocatalysts towards enhanced hydrogen evolution reaction in alkaline media. *Angew. Chem. Int Ed. Engl.* **60**, 259–267 (2021).
8. Mondal, P., Satra, J., Srivastava, D. N., Bhadu, G. R. & Adhikary, B. Pd$^{\delta+}$-mediated surface engineering of AgMnO$_4$ nanorods as advanced bifunctional electrocatalysts for highly efficient water electrolysis. *ACS Catal.* **11**, 3687–3703 (2021).
9. Wang, J. et al. Amorphization activated ruthenium-tellurium nanorods for efficient water splitting. *Nat. Commun.* **10**, 5692 (2019).
10. Chang, B., Hao, S., Ye, Z. & Yang, Y. A self-supported amorphous Ni-P alloy on a CuO nanowire array: an efficient 3D electrode catalyst for water splitting in alkaline media. *Chem. Commun.* **54**, 2393–2396 (2018).
11. Zhang, J. et al. Organic small molecule activates transition metal foam for efficient oxygen evolution reaction. *Adv. Mater.* **32**, e1906015 (2020).
12. Sun, J. et al. High throughput preparation of Ni–Mo alloy thin films as efficient bifunctional electrocatalysts for water splitting. *Int. J. Hydrog. Energy* **47**, 15764–15774 (2022).
13. Kwon, N. H. et al. A rational method to kinetically control the rate-determining step to explore efficient electrocatalysts for the oxygen evolution reaction. *NPG Asia Mater.* **10**, 659–669 (2018).
14. Li, W., Feng, B., Yi, L., Li, J. & Hu, W. Highly efficient alkaline water splitting with Ru-doped Co–V layered double hydroxide nanosheets as a bifunctional electrocatalyst. *ChemSusChem* **14**, 730–737 (2021).
15. Kwon, T. et al. Au-Ru alloy nanofibers as a highly stable and active bifunctional electrocatalyst for acidic water splitting. *Appl. Surf. Sci.* **563**, 150293 (2021).
16. Wang, L. et al. Rapid complete reconfiguration induced actual active species for industrial hydrogen evolution reaction. *Nat. Commun.* **13**, 5785 (2022).
17. Liao, C. et al. Constructing conductive interfaces between nickel oxide nanocrystals and polymer carbon nitride for efficient electrocatalytic oxygen evolution reaction. *Adv. Funct. Mater.* **29**, 1904020 (2019).
18. Jing, S. et al. Carbon-encapsulated WO$_x$ hybrids as efficient catalysts for hydrogen evolution. *Adv. Mater.* **30**, e1705979 (2018).
19. Xiao, Y. et al. Regulating the pore structure and oxygen vacancies of cobaltosic oxide hollow dodecahedra for an enhanced oxygen evolution reaction. *NPG Asia Mater.* **12**, 73 (2020).
20. Wang, D. et al. Atomic and electronic modulation of self-supported nickel-vanadium layered double hydroxide to accelerate water splitting kinetics. *Nat. Commun.* **10**, 3899 (2019).
21. Zhang, Y. et al. Constructing a multi-bishelled cobalt-based electrocatalyst for the oxygen evolution reaction in CO$_2$ electrolysis. *NPG Asia Mater.* **14**, 55 (2022).

22. Hao, Y.-R. et al. Tuning the electronic structure of CoP embedded in N-doped porous carbon nanocubes via Ru doping for efficient hydrogen evolution. *ACS Appl. Mater. Interfaces* **13**, 56035–56044 (2021).

23. Yin, H. et al. Ultrathin platinum nanowires grown on single-layered nickel hydroxide with high hydrogen evolution activity. *Nat. Commun.* **6**, 6430 (2015).

24. Li, S. et al. Modifying properties and endurance of CoP by cerium doping to enhances overall water splitting in alkaline medium. *J. Electroanal. Chem.* **922**, 116748 (2022).

25. Zhang, R. et al. Selective phosphidation: an effective strategy toward CoP/CeO$_2$ interface engineering for superior alkaline hydrogen evolution electrocatalysis. *J. Mater. Chem. A* **6**, 1985–1990 (2018).

26. Zhang, W., Descorme, C., Valverde, J. L. & Giroir-Fendler, A. Yttrium-modified Co$_3$O$_4$ as efficient catalysts for toluene and propane combustion: effect of yttrium content. *J. Hazard. Mater.* **437**, 129316 (2022).

27. Jia, Y. et al. Unique excavated rhombic dodecahedral PtCu$_3$ alloy nanocrystals constructed with ultrathin nanosheets of high-energy {110} facets. *J. Am. Chem. Soc.* **136**, 3748–3751 (2014).

28. Lu, Q. et al. Highly porous non-precious bimetallic electrocatalysts for efficient hydrogen evolution. *Nat. Commun.* **6**, 6567 (2015).

29. Jana, R., Bhim, A., Bothra, P., Pati, S. K. & Peter, S. C. Electrochemical dealloying of PdCu$_3$ nanoparticles to achieve Pt-like activity for the hydrogen evolution reaction. *ChemSusChem* **9**, 2922–2927 (2016).

30. Cobo, S. et al. A Janus cobalt-based catalytic material for electro-splitting of water. *Nat. Mater.* **11**, 802–807 (2012).

31. Li, Y. et al. MoS$_2$ nanoparticles grown on graphene: an advanced catalyst for the hydrogen evolution reaction. *J. Am. Chem. Soc.* **133**, 7296–7299 (2011).

32. Zhao, X., Zhu, H. & Yang, X. Amorphous carbon supported MoS$_2$ nanosheets as effective catalysts for electrocatalytic hydrogen evolution. *Nanoscale* **6**, 10680–10685 (2014).

33. Khan, Z. et al. Hierarchical urchin-shaped α-MnO$_2$ on graphene-coated carbon microfibers: a binder-free electrode for rechargeable aqueous Na–air battery. *NPG Asia Mater.* **8**, e294 (2016).

34. Shinde, S. S., Sami, A. & Lee, J.-H. Nitrogen- and phosphorus-doped nanoporous graphene/graphitic carbon nitride hybrids as efficient electrocatalysts for hydrogen evolution. *ChemCatChem* **7**, 3873–3880 (2015).

35. Ito, Y., Cong, W., Fujita, T., Tang, Z. & Chen, M. High catalytic activity of nitrogen and sulfur Co-doped nanoporous graphene in the hydrogen evolution reaction. *Angew. Chem. Int. Ed. Engl.* **54**, 2131–2136 (2015).

36. Konkena, B., Masa, J., Xia, W., Muhler, M. & Schuhmann, W. MoSSe@reduced graphene oxide nanocomposite heterostructures as efficient and stable electrocatalysts for the hydrogen evolution reaction. *Nano Energy* **29**, 46–53 (2016).

37. Zheng, Y. et al. Hydrogen evolution by a metal-free electrocatalyst. *Nat. Commun.* **5**, 3783 (2014).

38. Han, Q. et al. Mesh-on-mesh graphitic-C$_3$N$_4$@graphene for highly efficient hydrogen evolution. *Adv. Funct. Mater.* **27**, 1606352 (2017).

39. Cao, B. et al. Tailoring the d-band center of N-doped carbon nanotube arrays with Co$_4$N nanoparticles and single-atom Co for a superior hydrogen evolution reaction. *NPG Asia Mater.* **13**, 1 (2021).

40. Tan, Y. et al. Versatile nanoporous bimetallic phosphides towards electrochemical water splitting. *Energy Environ. Sci.* **9**, 2257–2261 (2016).

41. Park, J. et al. Investigation of the support effect in atomically dispersed Pt on WO$_{3-x}$ for utilization of Pt in the hydrogen evolution reaction. *Angew. Chem. Int. Ed. Engl.* **58**, 16038–16042 (2019).

42. Chen, J. et al. Reversible hydrogen spillover in Ru-WO$_{3-x}$ enhances hydrogen evolution activity in neutral pH water splitting. *Nat. Commun.* **13**, 5382 (2022).

43. Pei, Y. et al. RuCo alloy trifunctional electrocatalysts with ratio-dependent activity for Zn–air batteries and self-powered water splitting. *Chem. Commun.* **57**, 1498–1501 (2021).

44. Li, G. et al. The synergistic effect of Hf-O-Ru bonds and oxygen vacancies in Ru/HfO$_2$ for enhanced hydrogen evolution. *Nat. Commun.* **13**, 1270 (2022).

45. Du, R. et al. Unveiling reductant chemistry in fabricating noble metal aerogels for superior oxygen evolution and ethanol oxidation. *Nat. Commun.* **11**, 1590 (2020).

46. You, M. et al. In-situ growth of ruthenium-based nanostructure on carbon cloth for superior electrocatalytic activity towards HER and OER. *Appl. Catal. B Environ.* **317**, 121729 (2022).

47. Li, F. et al. Yttrium- and cerium-codoped ultrathin metal-organic framework nanosheet arrays for high-efficiency electrocatalytic overall water splitting. *Nano Lett.* **22**, 7238–7245 (2022).

48. Liu, Y. et al. 2D electron gas and oxygen vacancy induced high oxygen evolution performances for advanced Co$_3$O$_4$/CeO$_2$ nanohybrids. *Adv. Mater.* **31**, e1900062 (2019).

49. Yin, J. et al. NiCo$_2$O$_4$-based nanosheets with uniform 4 nm mesopores for excellent Zn-Air battery performance. *Adv. Mater.* **32**, e2001651 (2020).

50. Lei, L., Huang, D., Chen, Y., Chen, S. & Deng, R. Design of an amorphous and defect-rich CoMoOF layer as a pH-universal catalyst for the hydrogen evolution reaction. *J. Mater. Chem. A* **9**, 8730–8739 (2021).

51. Wang, Z. et al. Defect-rich nitrogen doped Co$_3$O$_4$/C porous nanocubes enable high-efficiency bifunctional oxygen electrocatalysis. *Adv. Funct. Mater.* **29**, 1902875 (2019).

52. Zhang, J. et al. Cation vacancy stabilization of single-atomic-site Pt$_1$/Ni(OH)$_x$ catalyst for diboration of alkynes and alkenes. *Nat. Commun.* **9**, 1002 (2018).

53. Li, G., Zheng, K., Li, W., He, Y. & Xu, C. Ultralow Ru-induced bimetal electrocatalysts with a Ru-enriched and mixed-valence surface anchored on a hollow carbon matrix for oxygen reduction and water splitting. *ACS Appl. Mater. Interfaces* **12**, 51437–51447 (2020).

54. Ling, T. et al. Activating cobalt(II) oxide nanorods for efficient electrocatalysis by strain engineering. *Nat. Commun.* **8**, 1509 (2017).

55. Wang, X. et al. CeO$_x$-decorated NiFe-layered double hydroxide for efficient alkaline hydrogen evolution by oxygen vacancy engineering. *ACS Appl. Mater. Interfaces* **10**, 35145–35153 (2018).

56. Zhao, Y. et al. Defect-engineered ultrathin δ-MnO$_2$ nanosheet arrays as bifunctional electrodes for efficient overall water splitting. *Adv. Energy Mater.* **7**, 1700005 (2017).

57. Ding, B. et al. Tuning the density of zero-field skyrmions and imaging the spin configuration in a two-dimensional Fe$_3$GeTe$_2$ magnet. *NPG Asia Mater.* **14**, 74 (2022).

58. Shi, W. et al. Vapor phase polymerization of Ag QD-embedded PEDOT film with enhanced thermoelectric and antibacterial properties. *NPG Asia Mater.* **14**, 47 (2022).

59. Liu, Y. et al. Large barocaloric effect in intermetallic La$_{1.2}$Ce$_{0.8}$Fe$_{11}$Si$_2$H$_{1.86}$ materials driven by low pressure. *NPG Asia Mater.* **14**, 30 (2022).

60. Huang, P. et al. Crystalline chirality and interlocked double hourglass Weyl fermion in polyhedra-intercalated transition metal dichalcogenides. *NPG Asia Mater.* **13**, 49 (2021).

61. Jiang, F., Choy, W. C., Li, X., Zhang, D. & Cheng, J. Post-treatment-free solution-processed non-stoichiometric NiO$_x$ nanoparticles for efficient hole-transport layers of organic optoelectronic devices. *Adv. Mater.* **27**, 2930–2937 (2015).

62. Joshi, A. et al. Synergistic incorporation of Fe and Co into nickel boride/NiCoHydroxide nanosheets to tune voltage plateau and charge storage in supercapacitors. *Electrochimica Acta.* **449**, 142144 (2023).

63. Li, K. et al. An ultrafast conducting polymer@MXene positive electrode with high volumetric capacitance for advanced asymmetric supercapacitors. *Small* **16**, e1906851 (2020).

64. Cui, X., Ren, P., Deng, D., Deng, J. & Bao, X. Single layer graphene encapsulating non-precious metals as high-performance electrocatalysts for water oxidation. *Energy Environ. Sci.* **9**, 123–129 (2016).

65. Yang, Y. et al. Non-precious alloy encapsulated in nitrogen-doped graphene layers derived from MOFs as an active and durable hydrogen evolution reaction catalyst. *Energy Environ. Sci.* **8**, 3563–3571 (2015).

66. Chen, Z. et al. Thermal migration towards constructing W-W dual-sites for boosted alkaline hydrogen evolution reaction. *Nat. Commun.* **13**, 763 (2022).

67. Zhang, T. et al. Pinpointing the axial ligand effect on platinum single-atomcatalyst towards efficient alkaline hydrogen evolution reaction. *Nat. Commun.* **13**, 6875 (2022).

68. Bai, X. et al. Integrating RuNi alloy in S-doped defective carbon for efficient hydrogen evolution in both acidic and alkaline media. *Chem. Eng. J.* **417**, 129319 (2021).

69. Liu, H. et al. Ultra-small Ru nanoparticles embedded on Fe–Ni(OH)$_2$ nanosheets for efficient water splitting at a large current density with long-term stability of 680 h. *J. Mater. Chem. A* **10**, 4817–4824 (2022).

70. Barman, B. K., Sarkar, B. & Nanda, K. K. Pd-coated Ru nanocrystals supported on N-doped graphene as HER and ORR electrocatalysts. *Chem. Commun.* **55**, 13928–13931 (2019).

71. Guo, J.-X. et al. High electrocatalytic hydrogen evolution activity on a coupled Ru and CoO hybrid electrocatalyst. *J. Energy Chem.* **37**, 143–147 (2019).

72. Zhang, J., Xu, X., Yang, L., Cheng, D. & Cao, D. Single-atom Ru doping induced phase transition of MoS$_2$ and S vacancy for hydrogen evolution reaction. *Small Methods* **3**, 1900653 (2019).

73. Creus, J. et al. Ligand-capped Ru nanoparticles as efficient electrocatalyst for the hydrogen evolution reaction. *ACS Catal.* **8**, 11094–11102 (2018).

74. Chen, W., Xie, Y., Gao, X., Li, L. & Lin, Z. Simultaneous optimization of CoIr alloy nanoparticles and 2D graphitic-N doped carbon support in CoIr@CN by Ir doping for enhanced oxygen and hydrogen evolution reactions. *J. Mater. Chem. A* **10**, 15543–15553 (2022).

75. Liu, N. et al. Bifunctional nanoporous ruthenium-nickel alloy nanowire electrocatalysts towards oxygen/hydrogen evolution reaction. *Int. J. Hydrog. Energy* **47**, 31330–31341 (2022).

76. Zhang, Y. et al. Nanostructured metal chalcogenides for energy storage and electrocatalysis. *Adv. Funct. Mater.* **27**, 1702317 (2017).

77. Qiu, B. et al. Fabrication of nickel–cobalt bimetal phosphide nanocages for enhanced oxygen evolution catalysis. *Adv. Funct. Mater.* **28**, 1706008 (2018).

78. Sheng, W., Myint, M., Chen, J. G. & Yan, Y. Correlating the hydrogen evolution reaction activity in alkaline electrolytes with the hydrogen binding energy on monometallic surfaces. *Energy Environ. Sci.* **6**, 1509–1512 (2013).

79. He, Q. et al. Achieving efficient alkaline hydrogen evolution reaction over a Ni_5P_4 catalyst incorporating single-atomic Ru sites. *Adv. Mater.* **32**, 1906972 (2020).

80. Liu, X. et al. Boosting electrochemical hydrogen evolution of porous metal phosphides nanosheets by coating defective TiO_2 overlayers. *Small* **14**, 1802755 (2018).

81. Li, Y. et al. Interstitial boron-triggered electron-deficient Os aerogels for enhanced pH-universal hydrogen evolution. *Nat. Commun.* **13**, 1143 (2022).

82. Tu, K. et al. A novel heterostructure based on RuMo nanoalloys and N-doped carbon as an efficient electrocatalyst for the hydrogen evolution reaction. *Adv. Mater.* **32**, 2005433 (2020).